Numerical investigation of biomass fast pyrolysis in a free fall reactor

ARTUR BIENIEK*
WOJCIECH JERZAK
ANETA MAGDZIARZ

AGH University of Science and Technology, Mickiewicza 30, 30-059, Krakow, Poland

Abstract This work presents two-dimensional numerical investigations of fast pyrolysis of red oak in a free fall reactor. The Euler–Lagrange ap-proach of multiphase flow theory was proposed in order to describe the behaviour of solid particles in the gaseous domain. The main goal of this study was to examine the impact of the flow rate of inert gas on the pyrol-ysis process. Calculation domain of the reactor was made according to data found in the literature review. Volume flow rates were 3, 9, 18, and 25 l/min, respectively. Nitrogen was selected as an inert gas. Biomass pyrolysis was conducted at 550°C with a constant mass flow rate of biomass particles equal to 1 kg/h. A parallel multistage reaction mechanism was applied for the thermal conversion of red oak particles. The composition of biomass was represented by three main pseudo-components: cellulose, hemicellulose and lignin. The received products of pyrolysis were designated into three groups: solid residue (char and unreacted particles), primary tars and non-condensable gases. In this work the impact of the volume flow rate on the heating time of solid particle, temperature distribution, yields and char mass fraction has been analysed. The numerical solutions were verified accord-ing to the literature results when the flow of nitrogen was set at 18 l/min. The calculated results showed that biomass particles could be heated for longer when the flow rate of nitrogen was reduced, allowing for a greater concentration of volatile matter.

Keywords: Fast pyrolysis; Biomass, Euler–Lagrange; Drop tube reactor; Heating time

1 Introduction

The World Biomass Association has published that the primary energy consumption for 2017, according to released data, supplied renewable energy sources of 81.1 EJ of primary energy, which corresponded to 13.9% in total energy production [1]. The highest content in green energy was biomass and its consumption was 55.6 EJ, which was 70% of renewable energy sources. These quantities indicate that biomass plays a significant role in power engineering, and its impact on the global energy sector is noticeable.

Biomass is an easily accessible renewable energy source due to its common occurrence in the environment. For many years, biomass has been used to produce heat, electricity and valuable fuels for use in man-made processes. The most popular method of biomass usage is combustion. The chemical energy included in biomass particles is released in exothermic reactions which enables the production of heat and, also, electricity in power plants. Other methods focus on the conversion of biomass feedstocks into valuable fuels as bio-oils, char and gases. One of these methods is pyrolysis: a process where long structures of biomass components are degraded under a high temperature (typically 350–700°C) in a non-oxygen atmosphere [2].

Pyrolysis is a very advanced method where some factors such as residence time, temperature, heating rate and also reactor geometry have a crucial impact on the process [3]. A combination of various parameters leads to obtaining different fuels in appropriate proportions. For example, a low temperature pyrolysis in a fixed bed reactor promotes the acquirement of more fraction of char, while under a high temperature in a fluidized bed reactor, bio–oil has the highest concentration [2, 4–7]. The fact that the pyrolysis process, under a number of conditions, delivers diverse fuels has become a subject of many scientific works. Nowadays, in many papers, it can be observed that experiments are supported by numerical calculations [8–15]. In those studies, research and analysis were conducted on the thermal conversion of solid particles. The numerical results were confirmed by experimental investigations. Moreover, the authors provided knowledge in the mathematical modelling of thermal processes.

Kaczor *et al.* [16] presented a comprehensive and detailed review concerning computational fluid dynamics (CFD) modelling in biomass pyrolysis, especially biomass pyrolysis via solar radiation. The most important information on biomass pyrolysis by CFD cal-culations; kinetic schemes of biomass pyrolysis are presented in the review. Additionally, the authors described approaches and models which are commonly used to simulate mul-tiphase behaviours in different reactors. One of which is the Euler-Euler multifluid model which is the most frequent method employed in numerical investigations [10, 17–19]. These models respect solid and fluid phases as a continuous medium with interactions between them, e.g. heat transfer, moment exchange, reaction, etc. Xue *et al.* [10,17] used this approach to calculate biomass fast pyrolysis in a fluidized bed reactor. The authors described a mathematical model of biomass particle pyrolysis in a fluidized reactor ac-cording to the governing equations of multifluid flow, where pure cellulose and red oak was used as a feedstock. They validated their results by experimental investigations and proved that vapour residence time and temperature have a significant influence on bio-oil. Yu *et al.* [18] employed the Euler-Euler model to calculate biomass pyrolysis in a downer reactor equipped with a novel solid separator and presented their method for separat-ing char particles from the gas phase after biomass fast pyrolysis. Furthermore, they examined the efficiency of the solid phase separation, which was around 99.9%. Mellin *et al.* [19] applied the CFD calculation with an Euler-Euler approach to simulate biomass

fast pyrolysis in a fluidized bed reactor. As a feedstock, researchers used a blend of spruce and pine. The scientists focused on maximizing the gaseous species, thereby proving that the application of higher temperatures decreases the tar fraction in the received prod-ucts. It was observed that the higher residence time of vapours slightly decreased the tar fraction.

Another approach to the numerical analysis of the multiphase flow of pyrolyzed biomass with inert gas is the Euler–Lagrange method, where biomass is considered as a solid discrete phase interacting with a continuous phase. Qi *et al.* [20] employed the Euler–Lagrange method to investigate biomass fast pyrolysis in a double auger reactor. They developed a CFD model to predict evolved species during pyrolysis, and their considerations were confirmed by experimental measurements, focusing on the calculation of the pyrolysis number. Pyrolysis number is defined as the ratio of the reaction rate to the heat transfer rate [21–23]. It was observed that for a particle size of 0.002 m, heat transport dominates. Ansarifar *et al.* [24] used the discrete phase model approach to investigate biomass gasification in a fluidized bed reactor. The authors focused on hydrogen production. They analysed the effect of hydrodynamics by varying the temperature of the bed and noticed inconsistent behaviour of the particles between hot and cold bed reactors.

Generally, the presented results concern macroscale investigations as well as the fundamental principles for a single particle. This may lead to a better understanding of the mechanism of biomass pyrolysis, and is currently under investigation [11, 25–27]. These works focus on interparticle reactions and also interactions in the fluid phase. Specifically, the pore size impact which is analysed on the conversion efficiency.

This paper presents the investigation of the biomass fast pyrolysis in a free fall reactor via numerical calculations. In this study, the impact of the volume flow rate of sweeping gas on the pyrolysis process was investigated. The selected flow rates were: 3, 9, 18, and 25 l/min. The Euler–Lagrange approach was involved in the multiphase flow. Yields of products, species and temperature distributions were analysed under various flow rates. The residence time under various conditions was plotted. Some of the numerical solutions have been validated with experimental data found in the literature review.

2 Materials and methods

2.1 Numerical model

2.1.1 Free fall reactor

Gable and Brown published a study of biomass fast pyrolysis in a free fall reactor [28]. They focused on examining the impact of biomass particle heating times on bio-oil yields. The laboratory setup was comprehensively described. A reactor was built consisting of two parts: the main part was a drop tube reactor complemented with an auxiliary auger reactor. An additional reactor helped to provide extra heating time when it was found necessary. This paper considered only the free fall reactor for all experiments performed. The experimental data was used in this study for numerical investigation and based on the data computational model on which it was built.

Figure 1 shows the reactor scheme employed from the published and developed numerical model. The free fall reactor was built from a stainless steel pipe. The inner diameter

(*d*) was 0.035 m and the total length of the reactor tube (L_T) was 3.05 m. The heating section, (*L*) was 2.77 m high. The cooling section (*H*) was added by the authors of this publication providing a further 3 m. The main reason was to thoroughly cool the prod-ucts of the pyrolysis process. Previously, the authors had assumed that the temperature of the products after cooling was the same as the surrounding temperature.

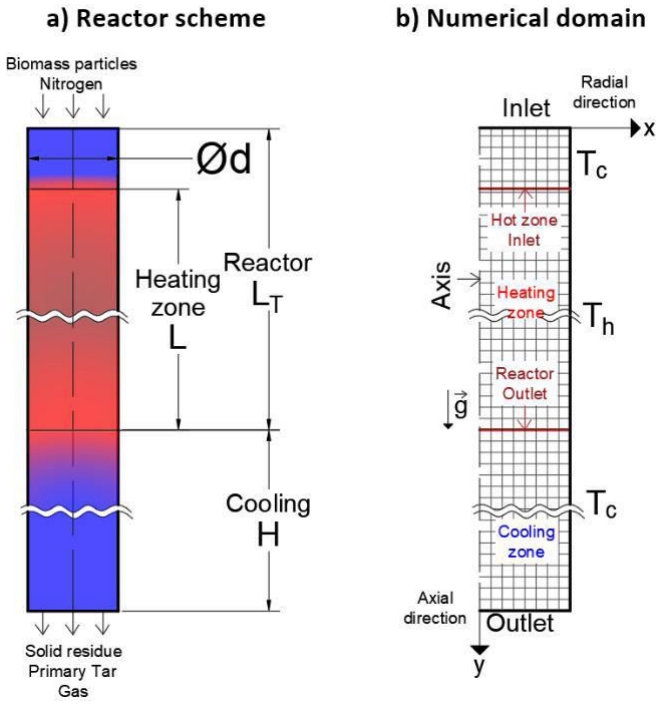

Figure 1: The reactor scheme and restored numerical model adopted [28].

2.1.2 Numerical domain and boundary conditions

In these studies, the numerical model geometry fully corresponds with the presented description. From the CFD calculations, the cooling section was deemed important due to the application of the pressure outlet boundary conditions, which refer to the process conditions. According to Fig. 1, at the inlet, the biomass mass flow rate was set at 1 kg/h at a temperature equal to 25˚C. The volume flow rate of nitrogen was from 3, 9, 18 to 25 l/min. The velocity inlet boundary condition was applied for nitrogen at: 0.052, 0.156, 0.312, and 0.433 m/s, respectively. The temperature of the nitrogen used was equal to 25˚C. The reactors had isothermal walls and their temperature was set at 550˚C (T_h) in the heating zone, and 25˚C at the beginning, and at the cooling sections (T_C). At the outlet, the pressure outlet boundary condition was set and the pressure and temperature of the surroundings were incorporated (101 325 Pa at 25˚C). The governing equations were solved in cylindrical coordinate system and, in the middle of the reactor,

the axis boundary condition was applied. Transient calculations were made and the initial temperature of 550˚C was set in all cells in the heating zone. The rest of the domain contains cells with a temperature equal to 25˚C.

2.2 Euler–Lagrange model

Biomass pyrolysis in a free fall reactor involves a flow of two separated phases (solid par-ticles and sweeping gas). The mathematical description requires a set of equations which can correctly solve any considered problem. The theory of multiphase flow is based on two approaches: Euler–Euler and Euler–Lagrange. The first method assumes both phases as interpenetrating continuous media in respect to Eulerian equations. The solid particles behaviour is supported by the kinetic theory of granular flow. The second model uses the Eulerian approach to describe fluid behaviour by solving the governing equation. The dispersed phase, as biomass particles, is modelled by the Lagrange approach, where a significant number of particles are tracked through the fluid flow field. The solid phase can exchange mass, momentum and energy with the fluid phase. Due to heterogenous reactions, species are also able to be transferred between phases. The basic assumption allows the use of this model when secondary phases occupy a relatively small volume fraction (typically less than 12%). A particle- particle interaction are neglected. Particles keep a distance and have a small probability for collision. The Euler–Lagrange multiphase model is often reported as a discrete phase model (DPM). The DPM delivers compre-hensive tools to track solid particles' trajectories. This approach has made it possible to learn about the behaviour of biomass particles under various flow rates of inert gas.

2.3 Governing equations

2.3.1 Eulerian phase

The Eulerian phase is assisted by a mixture of nitrogen and pyrolytic gases. The behaviour of the fluid flow is described by governing equations which refer to the conservation of mass, momentum, energy and species. The equations presented below were used in the calculations.

The conservation of mass for the fluid phase is described by

$$\frac{\partial \rho}{\partial t} + \mathrm{r} \cdot (\rho \sim v) = S_{DPM} + S_{\text{other}}, \tag{1}$$

where ρ is the density of the gaseous mixture, t refers to time, $\sim v$ is the velocity vector of the fluid phase, S_{DPM} is the mass exchange between gas and particles, and S_{other} is the external mass source.

The density of the gaseous phase was calculated by the incompressible gas law and is presented in form

$$\rho = \frac{p_{\text{op}}}{\frac{R}{M_W} T}, \tag{2}$$

where p_{op} is the operating pressure, R is the universal gas constant, M_W is the mass weighted molar mass of a gaseous mixture, and T is the absolute temperature.

The conservation of momentum for the Eulerian phase based on the Navier–Stokes equation

$$\frac{\partial(\rho\tilde{v})}{\partial t} + \nabla\cdot(\rho\tilde{v}\cdot\tilde{v}) = -\nabla p + \nabla\cdot\tau + \rho\tilde{g} + F_{DPM} + F_{\text{other}}, \quad (3)$$

where τ is the stress tensor, $\tilde{g}$ is the gravity, F_{DPM} is the force arising from the interaction with the Lagrangian phase and F_{other} is the force from an external source.

The stress tensor was calculated by

$$\tau = \mu_w \left[\nabla\cdot\tilde{v} + \nabla\cdot\tilde{v}^T - \frac{2}{3}\nabla\cdot\tilde{v}\, I\right], \quad (4)$$

where μ_w is the mass-weighted viscosity of fluid phase and I is the unit tensor, superscript T denotes the vector transpose. This equation considers the effect of volume dilation.

The energy balance of the fluid phase was calculated by formula

$$\frac{\partial(\rho E)}{\partial t} + \nabla\cdot[\tilde{v}(\rho E + p)] = \nabla\left[k\nabla T - \sum_i h_i J_i + (\tau\cdot\tilde{v})\right] + S_{DPM} + S_{\text{other}}, \quad (5)$$

where E is the internal energy of gaseous phase, k is the coefficient of thermal conductivity, h_i is the enthalpy of ith species of gaseous mixture, J_i is the vector of mass diffusivity of ith species, S_{DPM} is the fluid-particle heat exchange, and S_{other} is the external heat source, e.g. chemical reaction.

The internal energy was calculated by

$$E = h - \frac{p}{\rho} + \frac{V^2}{2}. \quad (6)$$

The sensible enthalpy was calculated by the following equation:

$$h = \sum Y_i h_i + \frac{p}{\rho}, \quad (7)$$

where Y_i is the concentration of ith species, and h_i is the sensible enthalpy of ith component.

The sensible enthalpy of ith component was computed by

$$h_i = \int_{T_{\text{ref}}}^{T} c_{p,i}\, dT, \quad (8)$$

where $c_{p,i}$ is the constant pressure heat capacity of ith species, and T_{ref} is the reference temperature equal to 298 K (25°C).

Due to multicomponent fluid flow, species convection-diffusion equations were solved and the formula employed for each component has been presented as follows:

$$\frac{\partial(\rho Y_i)}{\partial t} + \nabla\cdot(\rho\tilde{v}Y_i) = -\nabla\cdot J_i + R_i + S_{DPM,i} + S_{\text{other},i}, \quad (9)$$

where R_i is the rate of creation of ith species due to the homogenous reaction, $S_{DPM,i}$ is the exchange rate of ith species between the fluid phase and dispersed phase by heterogenous reaction, and $S_{\text{other},i}$ is the external source of ith component.

The diffusion flux of *i*th component which arises from the concentration gradient and temperature can be calculated using Fick's law

$$\tilde{J}_i = -\rho D_{m,i} \nabla Y_i - D_{T,i} \frac{\nabla T}{T}, \quad (10)$$

where $D_{m,i}$ is the coefficient of mass diffusion, $D_{T,i}$ is the coefficient of thermal diffusion. These coefficients were calculated using the kinetic theory of gases [29, 30].

2.3.2 Lagrangian phase

The motion of solid particles in a fluid field is tracked when Newton's second law of dynamics is applied. This law considers all forces which act on the particle as drag force, gravity, virtual mass and other external forces. The force balance of the dispersed phase in respect to the second law of dynamics is

$$\frac{d\tilde{v}_p}{dt} = F_D(\tilde{v} - \tilde{v}_p) + \frac{\tilde{g}(\rho_p - \rho)}{\rho_p} + \tilde{F}, \quad (11)$$

where $\tilde{v}_p$ refers to the particle velocity vector, F_D is the drag force, ρ_p is the particle density, F_x is the virtual mass force, and F is the sum of other external forces. The particle-particle interactions are neglected due to a small volume fraction of biomass particles in the gaseous phase.

The drag force was calculated using equation

$$F_D = \frac{18\mu_w C_D \mathrm{Re}_s}{24\rho_p d_p^2}, \quad (12)$$

where C_D is the drag coefficient, Re_s is the Reynolds number for the solid particle, and d_p is the particle diameter.

The drag coefficient was estimated using the Wen–Yu model [31]

$$C_D = \frac{24}{\alpha_l \mathrm{Re}_s \left(1 + 0.15(\alpha_l \mathrm{Re}_s)^{0.687}\right)}, \quad (13)$$

where α_l corresponds to the volume fraction of the fluid phase.

The Reynolds number for the solid phase was computed by formula

$$\mathrm{Re}_s = \frac{\rho d_p |\tilde{v}_p - \tilde{v}|}{\mu}. \quad (14)$$

The virtual mass force was computed by

$$F_x = 0.5\,\rho_p \frac{d}{dt}(\tilde{v} - \tilde{v}_p). \quad (15)$$

The heat equation of the solid phase was determined when the heat balance for a single particle was considered. The total heat accumulated inside the particle was equal to the heat which was transferred from the continuous phase or other sources via convection, and heterogeneous reactions. The heat balance which was adopted for these numerical calculations presents the equation

$$m_p c_p \frac{dT_p}{dt} = aA_p(T_\infty - T_p) - \frac{dm_p}{dt} H_{\text{reaction}}, \quad (16)$$

where m_p is the particle mass, c_p is the heat capacity of the particle, T_p is the particle temperature, a is the heat transfer coefficient, A_p is the particle surface area, T_∞ is the temperature of fluid near the particle, and H_{reaction} is the enthalpy of the heterogeneous reaction.

The heat transfer coefficient a was computed using Nusselt's number correlation. The value of this number was determined *via* the Ranz–Marshall correlation [32] *via* the formula

$$\frac{}{k_\infty}$$

where k_∞ is the coefficient of the thermal conductivity of fluid around the biomass particle, and Pr is the fluid Prandtl number.

The mass of solid particles was calculated according to formula

$$m_p = \sum_{i=1}^{n} Y_i \rho_i \frac{4\pi d_p^3}{3}, \tag{18}$$

where Y_i is the concentration of ith compound which builds the biomass structure and ρ_i is the density of ith compound, and n is the number of compounds building the biomass structure.

The conversion rate of biomass particles was computed by equation

$$\frac{dm}{dt}^p = -m_p \sum^{n} X_j R_j, \tag{19}$$

where R_j is the surface reaction rate of ith reaction.

2.4 Reaction kinetic and material properties

The CFD computation of biomass pyrolysis requires the adaptation of a mechanism which involves the main reactions during solid particle conversion. Biomass pyrolysis is an extremely complex process where a huge amount of reactions occur and it is not possible to establish an universal model which could predict, precisely, the concentration of each component released during thermal degradation. However, CFD modelling has been successfully employed in estimating the yields of biomass pyrolysis products such as solid residues, primary tars and non-condensable gases, for various reaction schemes [16, 33–36]. Reaction models are classified into different subclasses and these consist of single step reactions, parallel single step reactions, single multistage reactions, and parallel multistage reactions. The latter is the best known type of reaction mechanism and was developed by Ranzi *et al.* [33].

In the presented paper, the model proposed by Miller and Bellan [34] was used and the scheme of this mechanism is presented in Fig. 2.

The proposed kinetic mechanism considers biomass particles as a composition of three main pseudo components, namely cellulose, hemicellulose and lignin. This kinetic scheme is based on parallel multistage first order reactions. In the first step, each component reacts to its active form. In the next stage it converts in a parallel reaction to primary tars, gas and chars. The mechanism also involves the independent reaction of primary tars cracking. Products of pyrolysis are categorized into three groups: solid residues (char), non-condensable gases and primary tars (condensable hydrocarbons). The reaction rate

Figure 2: Reaction mechanism of pyrolysis (where x is the mass fraction and $k_1, \ldots k_4$ are the kinetics rates of reaction of cellulose, hemicellulose, lignin, and tar, respectively).

(k) of each reaction is dependent on temperature, and the Arrhenius theory could be used to determine it. The particle surface reaction rate was computed according to equation

$$\overline{\mathrm{R}}_j = \eta Y_j k\,, \tag{20}$$

where $\overline{\mathrm{R}}_j$ is the particle surface reaction rate of jth biomass component, η is the dimensionless effectiveness factor set to 1, Y_j is the concentration of jth biomass compound on the surface, and k is the kinetic rate of reaction, which was calculated according to the Arrhenius theory

$$k = A_r T_p^{\gamma}\, e^{-\frac{E_a}{RT_p}}\,, \tag{21}$$

where A_r is the pre-exponential factor, T_p is the particle temperature, γ is the dimensionless temperature exponent, and E_a is the activation energy.

All required constant values applied to determine the reaction rates are listed in Table 1.

Table 1: Pre-exponential factor, activation energy and enthalpy of pyrolysis reaction [31].

Component	Reaction rate	x	A_r (s^{-1})	E_a (kJ mol^{-1})	$H_{reaction}$ (kJ kg^{-1})
Cellulose	k_1		2.8×10^{19}	242.2	0
	k_2		3.28×10^{14}	196.5	255
	k_3	0.35	1.3×10^{10}	150.5	–20
Hemicellulose	k_1		2.1×10^{16}	186.7	0
	k_2		8.75×10^{15}	202.4	255
	k_3	0.6	2.6×10^{11}	145.7	–20
Lignin	k_1		9.6×10^{8}	107.6	0
	k_2		1.5×10^{9}	143.8	255
	k_3	0.75	7.7×10^{6}	111.4	–20
Tar	k_4		4.28×10^{6}	108.0	–42

Red oak is composed of 50.9% of cellulose, 26.9% of hemicellulose and 22.2% of lignin [37]. The properties of the materials, which were included in CFD modelling, are presented in Table 2.

In the calculations, the apparent density of solid particles was incorporated. Almost all of the properties were constant, and did not depend on temperature. The density of inert gas and volatiles changed in respect to the incompressible ideal gas law.

Table 2: Data used for numerical calculations [34].

Properties	Eulerian phase			Lagrangian phase	
	Nitrogen	Tar	Gas	Red oak	Char
Pressure, p	Ideal gas law			650	350
Molar mass, M	28	100	30	162	12
Heat capacity, c_p	824.6	2500	1100	2300	1100
Thermal conductivity, k	0.0563	0.02557	0.02557	0.1256	0.0837
Viscosity, μ	3.58×10^{-5}	3×10^{-5}	3×10^{-5}	–	–
Coefficient of mass diffusivity, D_m, Coefficient of thermal diffusivity, D_T	Kinetic theory of gases			–	–
Diameter, d	–	–	–	0.0005	–

3 Results

3.1 Solution strategy

The governing equations were solved in the cylindrical frame using research software, An-sys Fluent 20R2 [38], where the finite elements' method was employed for two-dimensional analysis. The workstation was equipped with a 4 core processor with a maximum clock speed of 3.8 GHz and a cache memory of 6 MB, while the computer had 16 GB RAM of memory. Equations were calculated according to the block diagram which is shown in Fig. 3.

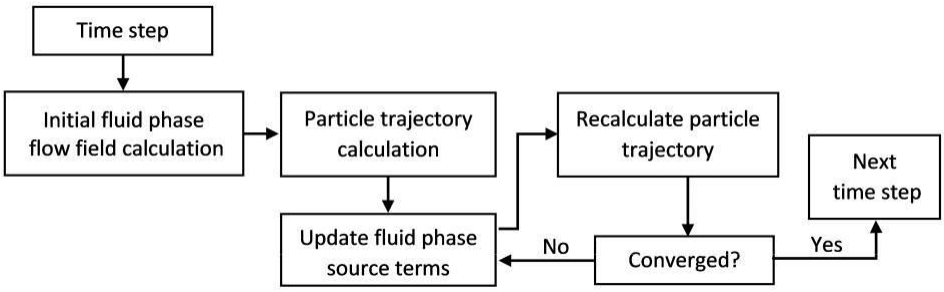

Figure 3: Algorithm of discrete phase model.

In the first step, the calculations solved variables within the fluid field. Then, the discrete elements were introduced to the fluid zone and their trajectories were computed. In the next stage, the source terms of mass, momentum, and energy from solid-fluid interactions were added to the right side of the governing equations and the field of continuous phase was recalculated. After recalculation, particle trajectories were computed once again and when any changes were lower than the convergences criteria, the model was computed for the next time step. Otherwise, the flow field was solved until solutions converged or the number of iterations per time step reached a limit.

The discretization scheme of pressure-velocity was set at coupled. The second order upwind discretization method was applied to momentum, energy, and species equations to achieve more accurate solutions. The residual value for continuity was set at 10^{-3} and for other equations it was 10^{-4}. The maximum number of iterations was 30 per time step, and particle trajectories were updated every 10 iterations.

3.2 Model validation

Transient calculations were performed and the total computed time was 5 or 7 s. The physical time needed to compute one case was around 20 hours. According to Figs. 4 and 5, the respected problem was supposed to steady conditions, but variables did not

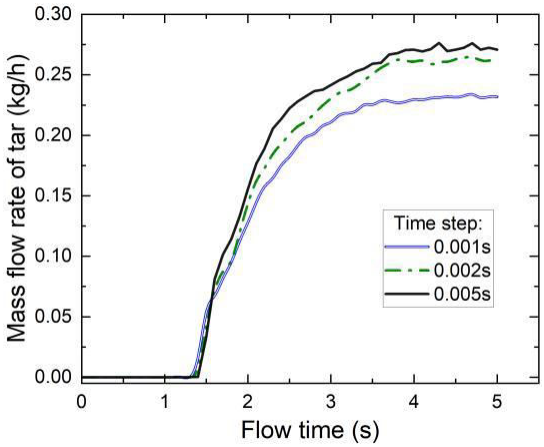

Figure 4: Time step dependency test.

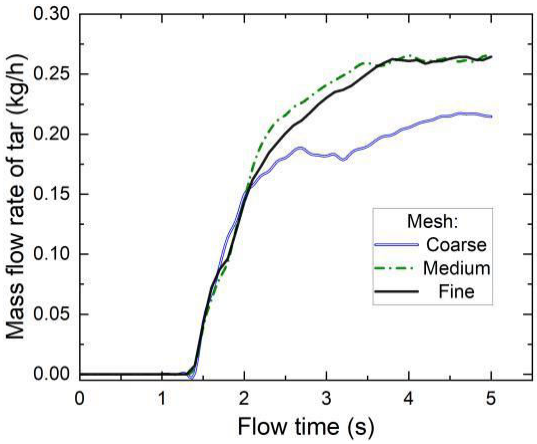

Figure 5: Mesh dependency test.

change significantly after a few seconds. A model sensitivity test was executed and three different time steps and meshes were performed. The entire computed zone had uniform elements and the number of elements was dependent on the quality of the mesh. In Table 3, the specific characterization of the involved meshes is presented. According to the quantity of generated elements, meshes were named as follows: coarse with 22 605 elements, medium with 40 140 elements and fine, which had the highest number of elements equal to 60 175.

Table 3: Characteristics of meshes involved in CFD studies.

Mesh	Element type	Element size (mm)	Min. orthogonal quality	Max. skewness	Max. aspect ratio	Total generated elements
Coarse	Quadrilateral	1.2×4	0.52	0.073	3.43	22 605
Medium	Quadrilateral	0.875 × 3	0.99	0.054	3.43	40 140
Fine	Quadrilateral	0.7 × 2.5	0.99	0.045	3.59	60 175

There were no significant differences between medium and fine mesh except for the quan-tity. Both meshes were of very good quality based on the orthogonal quality factor, Whereas, the coarse mesh had a lower orthogonal quality than the others, but this value still remained in the appropriate range which was supposed to be higher than 0.01.

The tested time steps were set at: 1×10^{-3} s, 2×10^{-3} s and 5×10^{-3} s. Time step dependency tests were made when the finest mesh was adapted. Mesh impact tests were studied for the time step and were equal to 2×10^{-3} s. In Figs. 4 and 5, the obtained solutions have been presented. Tests were made when the volume flow rate of nitrogen was 18 l/min. At the reactor outlet, the mass flow rate of primary tars was monitored in function of time. Results from each test were compared.

The analysis of time step impact showed that time steps of 2×10^{-3} s and 5×10^{-3} s led to similar solutions. The mass flow rate of tars at the reactor outlet corresponded to previous literature [28]. Calculations for the time step of 1×10^{-3} produced results which were different in comparison to earlier cases. The reduction of the time step decreased the mass flow rate of the condensable fraction (tars). The influence of mesh is presented in Fig. 5. It can be observed that medium and fine mesh converge to the same result. The coarse mesh allowed for significantly different solutions to be obtained despite the mass flow rate of tars increasing at the same rate for two seconds. Based on the received results and the mesh quality, further investigations were conducted with a fine mesh resolution and a time step of 2×10^{-3} s. The following cases involved 3 l/min, 9 l/min, 18 l/min and 25 l/min of volume flow rate of nitrogen. Figure 6 presents the development of primary tars and their quantity at the end of the reactor.

The presented solutions confirm that steady conditions for fluid phase variables could be observed after a few seconds in all considered cases, which have been mentioned previously. The mass flow rate of primary tars was stabilized, but significant changes were not recorded. The calculations were stopped at 5 s, except for the 3 l/min flow rate A verification of the model was made and the results are shown in Fig. 7. Product yields from the numerical study and the experiment investigation were compared under 18 l/min flow rate.

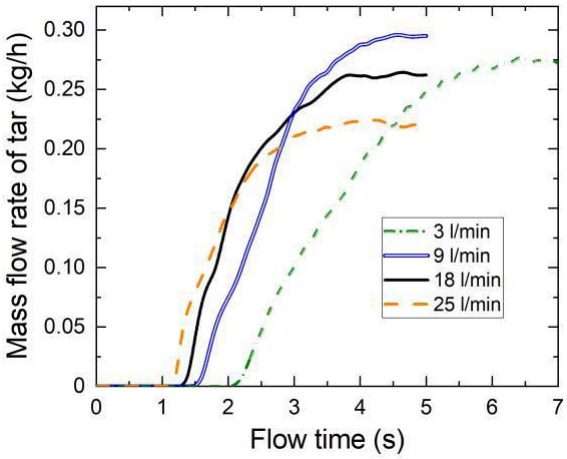

Figure 6: Mass flow rate of primary tar development in function of flow time.

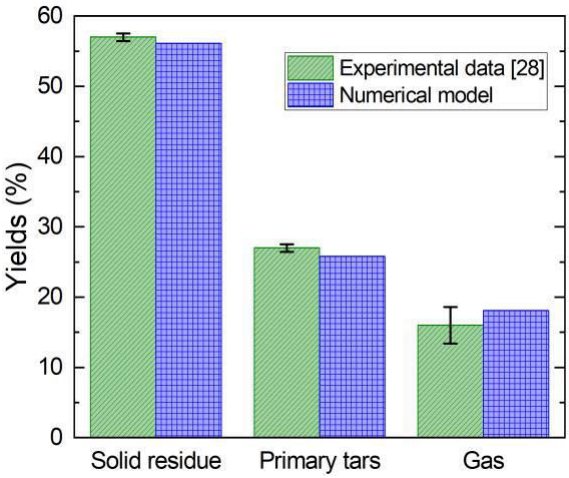

Figure 7: Comparison of numerical and experimental results.

The adopted calculation model satisfactorily reflected the experimental results [28]. Yields of all products were almost the same in both investigations. A low disproportion could be observed for non-condensable gases, but the numerical value of the yield remains in the range of error. According to [25], values of errors were 0.545% for solid and liquid fraction, and 2.6% for the gaseous phase.

The thermophysical properties of biomass and its products are limited for CFD calculations and, additionally, many assumptions were made to simplify the calculation process. Thus, there is a significant opportunity to develop a model which will provide good support for experiments, which has been proved.

3.3 Particle heating time

Gable and Brown introduced the idea of heating time [28]. The authors defined this concept as: a total average residence time of a single biomass particle in the reactor zone. It is important that the reactor zone is considered a place where heat is supplied to particles. They proposed a method for calculating this: the heating time is the length of the reactor divided by an average particle velocity. The particle velocity is a sum of the terminal of the particle and the velocity of inert gas. According to their calculations, the heating time was 1.4 s for 18 l/min.

Figure 8 presents the impact of the flow rate of nitrogen on the particle heating time. A simple characteristic was plotted to examine what the heating time would be if the volume flow rate changes. Determination of the heating time was measured using Eq. (11), when all force acting on the particles was respected. The heating time was computed as an average time in which biomass particles remained in the reactor zone.

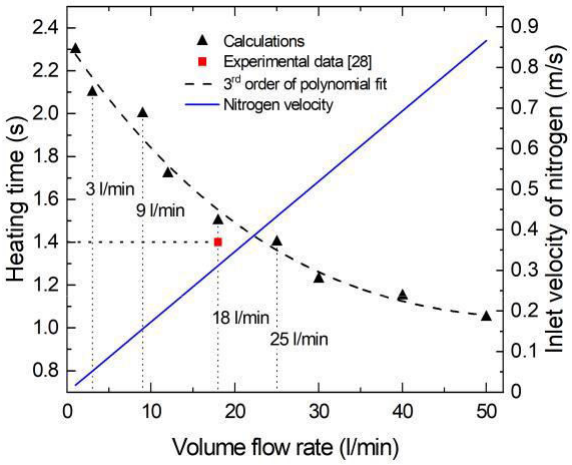

Figure 8: Heating time of biomass particle in function of volume flow rate.

The increase of volume flow rate of sweeping gas caused a linear growth of velocity in the inert gas at the reactor inlet. Figure 8 indicates that a higher velocity of nitrogen occurred as faster particles left the hot zone, and its residence time was shorter. More momentum was transferred from fluid to particles during interactions and because of this the particles accelerated to a higher speed. However, the higher velocity particles achieved a higher drag force, which slowed them down. The drag force included the particle velocity and its value increased proportionally to this velocity. The heating time was decreased non – linear and the 3rd order polynomial was proposed to fit data points.

Based on the numerical results, 1.5 s of average residence time of particles was obtained, while experimental results reported 1.4 s. These are very similar values but a small difference between them can be observed. Pyrolysis is a rapid process and in a split sec-ond a portion of the particle could be converted, and that is why some complex equations were included.

3.4 Reactor temperature

It was assumed that a steady flow after a few seconds and variables such as mass flow rate of species, mass average temperature and particle distribution did not change through the domain. This assumption allowed for the analysis of the distribution of properties at every point in the reactor. Dimensionless variables were introduced to the reactor zone and only there was analysis made. The cooling zone was disregarded because the authors did not expect pyrolysis reactions, and only cooling of the products took place there. The dimensionless axial length of the hot zone of the reactor was calculated according to

$$y^* = \frac{y - y_0}{L}, \tag{22}$$

where y is the axial coordinate, y_0 is the axial coordinate at the inlet of the hot zone, and L is the length of the heating section of the reactor. The dimensionless radial width of the reactor was calculated by

$$x^* = \frac{x - x_0}{R}, \tag{23}$$

where x is the radial coordinate, x_0 is the radial coordinate at the inlet of hot zone, and R is the radius of the reactor.

Figure 9 presents a fluid phase temperature distribution along the axial length of the reactor. Temperature profiles were plotted for four cases of volume flow rate of nitrogen. The temperature was measured in two ways. In the first method, the temperature was collected along the axis. The second approach involved a mass-weighted average across the pipe at specified axial points. These points were established from the hot zone inlet to the reactor outlet. The mass-weighted average temperature across the surface was calculated *via*

$$\frac{\int T \rho \tilde{v} \, d\tilde{A}}{\int} \quad \frac{\sum_{i=1}^{n} T_i \rho_i \tilde{v}_i \, d\tilde{A}_i}{\sum_{i=1}^{n} \rho_i \tilde{v}_i \, d\tilde{A}_i}$$

where T_i is the cell temperature, $\tilde{v}_i$ is the velocity of cell, A_i is the surface area of a single cell, and n is the total number of cells.

According to the presented results, it can be seen that the volume flow rate had an impact on temperature distribution throughout the reactor. The lower flow rate caused the higher temperature of fluid phases at the end of the reactor. At the end of the heat-ing zone, the average temperature of the gaseous phase had increased by approximately 100˚C when the flow rate was lowered from 25 to 3 l/min. This situation happened because the gaseous phase had more time to exchange heat with an isothermal wall. Additionally, at the last section of the reactor, the temperature gradient was the low-est when a lesser flow rate was set. The recorded difference between axial and average temperatures was the lowest. Another situation occurred at the beginning of the reactor. A higher flow rate of inert gas caused differences between average and axial temperatures, which were the lowest.

The temperature distribution had a crucial impact on the pyrolysis process. Particles which appeared closer to the hot wall had pyrolyzed faster due to interactions with the hot fluid and the wall. The rate of pyrolysis dropped along the radius, and in the axis

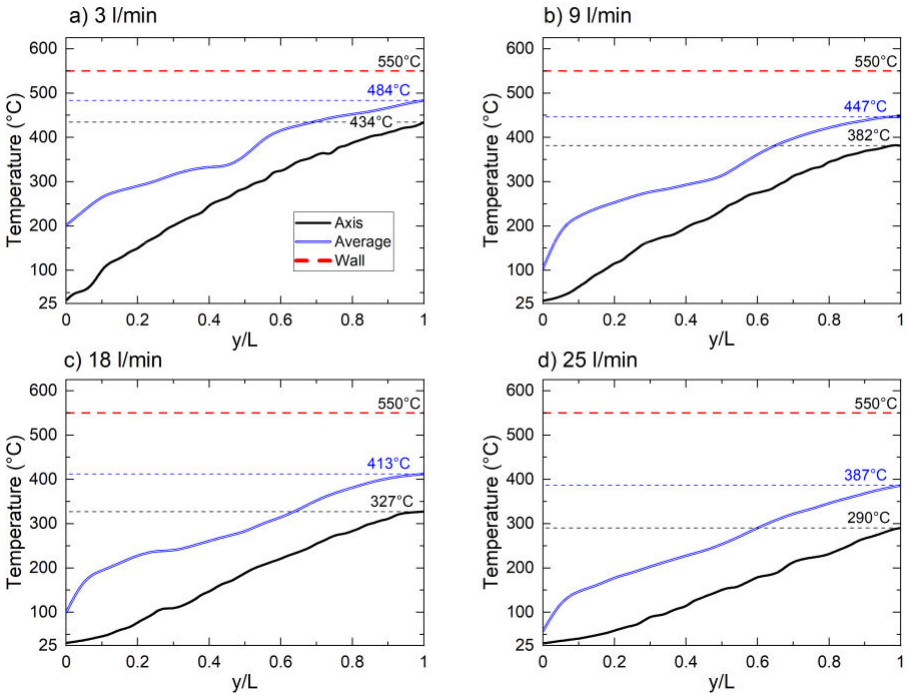

Figure 9: Fluid phase temperature distribution in the heated zone of the reactor.

was the lowest. A higher temperature in the axis could be achieved more quickly when a smaller flow rate of inert gas is used.

3.5 Particle position and temperature

Discrete phase distribution in the heated zone is presented in Fig 10. This figure contains information concerning trajectories, concentrations and the temperature of the dispersed phase. For better visualization of results, the reactor was divided into 4 parts due to the high ratio of reactor length to its radius (L $2R$, R – radius of the reactor). The particles are depicted when the discrete phase reached 25%, 50%, 75%, and around 100% of the total heated zone length. The particle distribution was mirrored along the y-axis due to cylindrical coordinates. Symmetrical results are considered because of laminar flow, whereas turbulence was not expected.

First of all, the concentration of biomass particles in the considered space should be analysed. In all cases the discrete phase took place close to the hot walls of the entire reactor. As the reactor length increased, more particles were recorded close to the walls. Another consideration is the volume flow rate impact on a total number of particles. It could be observed that for 3 l/min of flow rate of nitrogen there was a higher quantity of solid phase. This amount reduced when the flow rate was higher. At a constant mass flow rate of biomass, a greater velocity of gas caused the particles to be transported faster.

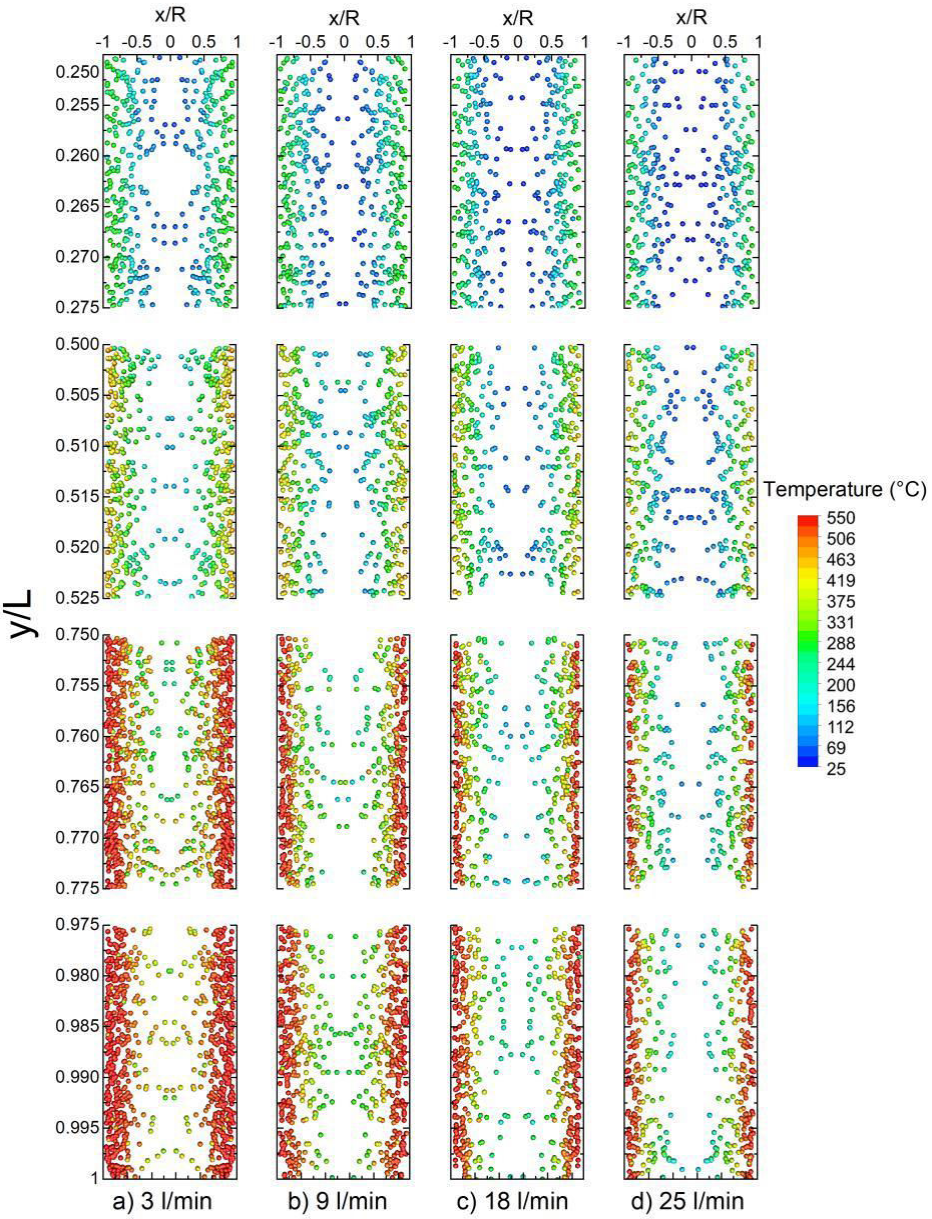

Figure 10: Particle position and temperature in the heated zone.

The residence time of the particles in the reactor zone was shortened. Alongside the reactor, biomass particles gained more heat leading to the highest temperatures at the end. Across the pipe, a noticeable gradient of temperature, where particle temperature

corresponded to fluid temperature, was recorded. An inert gas was also a heat carrier and its temperature influenced the particle temperature. For this reason, a lower temperature was monitored in the axis, while the temperature increased towards the hot walls.

3.6 Product evolution

Figure 11 depicts the species forming in the reactor hot zone for the investigated volume flow rates of nitrogen. An increase in the yield of volatile matter along the entire reactor was plotted. Data were collected at specified reactor points, where the mass-weighted av-erage of considered variables was computed. Additionally, the diagrams show the average conversion degree of the discrete phase.

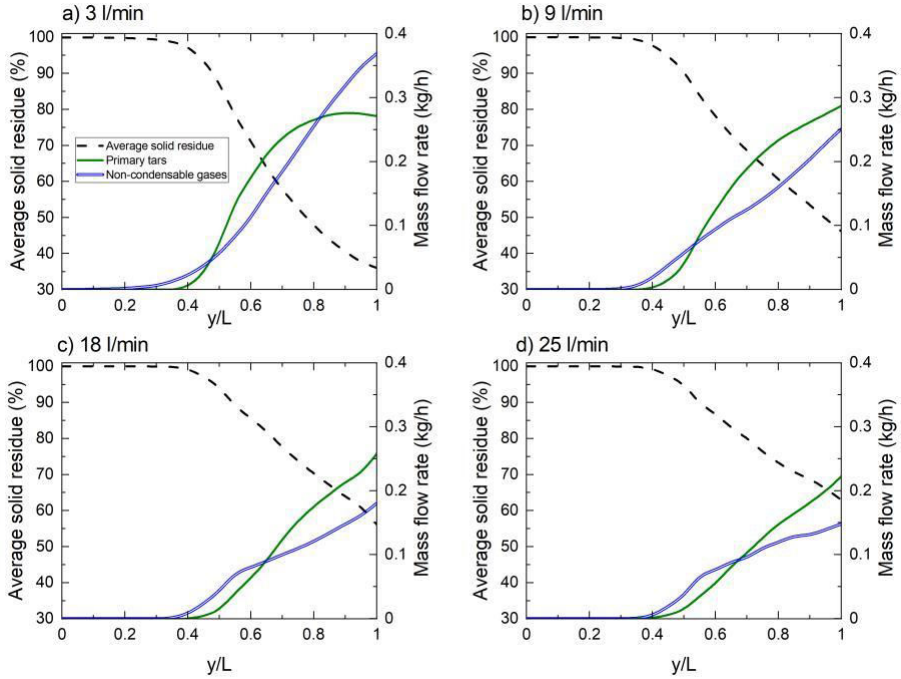

Figure 11: Evolution of pyrolysis products in the heating section of free fall reactor.

The dispersed phase began to convert when 40% of the reactor length was achieved. This situation was spotted in all variants of the inert gas flow rate. It could be assumed that in the first sections of the reactor the heat was supplied to biomass only. Temperature of the solid particles rose until the temperature of pyrolysis was reached. It is worth noticing that some particles could be found close to the hot walls and their temperature could be much higher than others. However, this analysis considered the average conversion rate at specified axial positions. In the other sections of the reactor, the degree of conversion was dependent on the volume flow rate of nitrogen. A lower flow of nitrogen caused more biomass particles to convert.

A mass flow rate of volatile species increased throughout the whole reactor. A lower flow rate of nitrogen caused a higher number of the mass flow rate of volatiles. A primary tar concentration was the highest at the end of the reactor for all cases expect the situation when the flow rate of nitrogen was 3 l/min. Under this condition, the primary tar flow rate displayed the greatest value at the 80% point of the reactor. Then its concentration started to decrease, which was due to thermal cracking reactions. With the lower volume flow rate, the primary tars developed less velocity and remained longer in the heated zone. Tars started to be broken up into non-condensable gases while the concentration increased.

A final yield of pyrolysis products is presented in Fig. 12. The required data were collected at the reactor outlet. The yields were determined *via* equation

$$\text{yield} = \frac{\int_{\text{outlet}} \rho v A Y \, dA}{\dot{m}_{\text{biomass, inlet}}} \times 100\%, \tag{25}$$

where ρ is the local density of the fluid phase, v is the velocity of gas, A is the surface area of a reactor outlet and Y is the concentration of a gaseous pyrolysis product. The obtained mass flow rate of selected species was divided by the initial mass flow rate of biomass particles ($\dot{m}_{\text{biomass, inlet}}$).

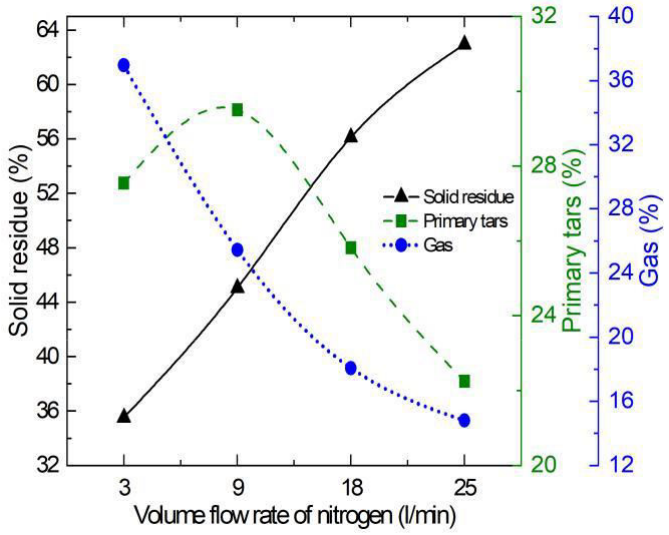

Figure 12: Yield of pyrolytic products.

From Fig. 12 it can be observed that a higher flow rate of sweeping gas decreased the amount of primary tars and non-condensable gases, while the fraction of the solid residue increased. Moreover, this chart suggests that there was some point of volume flow rate where the evolution of primary tars from red oak was the highest. Reducing the inert gas flow rate below this point led to the acquirement of additional non-condensable gases,

mainly due to thermal cracking. Generally, fast pyrolysis is a process which is primarily focused on bio-oil production [38–42]. It is worth considering all methods which lead to maximization of liquid fraction in pyrolytic products.

3.7 Particle conversion

Figure 13 shows the positions of the discrete phase at the end of the reactor. It should be explained that the char fraction does not refer to pure carbon. It provides knowledge about particle potential for pyrolysis. The value 0 means that the biomass particle contains maximum volatile matter. Whereas, value 1 provides information that a biomass particle is fully converted, and it will not release any further gaseous species.

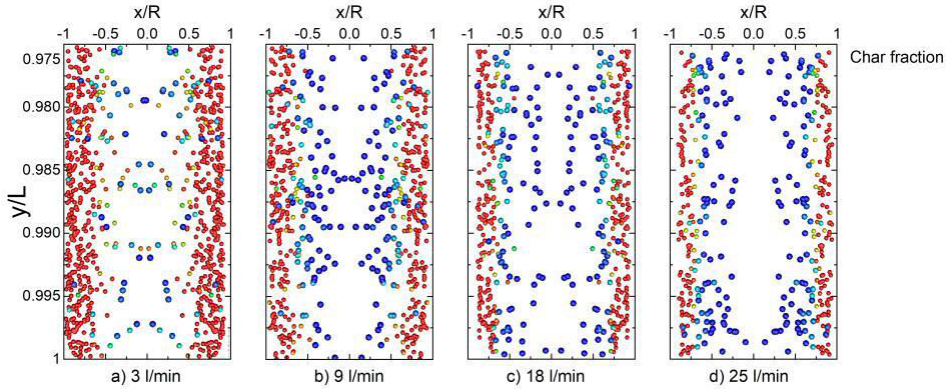

Figure 13: Mass fraction of char at the reactor outlet.

At the end of the reactor a significant quantity of particles were situated close to the walls where they fully released the volatile matter. The conversion certainly referred to temperature, where in this area particles were capable of obtaining its highest values. In the result, the particles were able to pyrolyze faster, thereby producing more char fraction. Numerical solutions showed that in all cases the lowest mass fraction of char in particles was in the axis. Towards the axis of the pipe, the mass fraction of char dropped and some unreacted particles were observed. The drop was dependent on the nitrogen flow rate. A higher flow of inert gas caused an increase in unconverted particles.

4 Conclusions

Numerical studies of the fast pyrolysis of biomass in a free fall reactor, based on a La-grangian approach (discrete phase model), were made. The effect of the volume flow rate of an inert gas on the pyrolysis process was investigated. A part of the computed solu-tions were verified with experimental results, and the obtained results were converged. Numerical investigations confirmed that the volume flow rate of sweeping gas influenced the particle residence time, which corresponded to the particle heating time. The higher the flow rate, the higher velocity of inert gas was developed and further momentum was transferred to the dispersed phase. The solid particles remained for a shorter time in

the reactor when the flow rate of the inert gas was higher. The solid phase increased its velocity, but the drag force also increased, which resisted particles. Decreasing the volume flow rate from 25 l/min to 3 l/min allowed an extension in the heating time of solid particles from 1.4 s to 2.3 s.

The temperature distribution in the heated zone was dependent on a flow rate of sweeping gas. At the end of the heating zone, the average temperature of the gaseous phase was 483°C at 3 l/min and it dropped to 386.5°C for 25 l/min. The lower volume flow rate had an influence on higher temperatures of the reactor, which led to an increase in the char fraction in raw particles. Analysis of the yields of products illustrated that more volatile species were obtained when the volume flow rate was reduced. The solid fraction reduced from 63% to 35.5% when the volume flow rate dropped. At the lowest flow rate, it was possible to maximize the conversion of biomass particles. Decreasing the volume of the flow rate of sweeping gas to some level enabled the production of more bio-oil fraction. Below this point, secondary reactions were observed where primary tars were broken down into gas fraction. The yield of non-condensable gases rose as long as the flow rate of sweeping gas fell. The maximal production of gas was expected in the absence of forced convection: only the free fall of solid particles in an inert atmosphere.

Acknowledgements This work was supported by the Ministry of Science and Higher Education, Poland, Grant AGH no. 16.16.110.663.

Received 17 March 2021

References

[1] *Global Bioenergy Statistics 2019*. World Biomass Association. http://www.worldbioenergy.org (accessed 1 March 2021).

[2] Basu P.: *Biomass Gasification, Pyrolysis and Torrefaction: Practical Design and Theory*. Elsevier, 2013.

[3] Tripathi M., Sahu J.N., Ganesan P.: *Effect of process parameters on production of biochar from biomass waste through pyrolysis: A review*. Renew. Sust. Energ. Rev. **55**(2016), 467–481.

[4] Lu J.S., Chang Y., Poon C.S., Lee D.J.: *Slow pyrolysis of municipal solid waste (MSW): A review*. Bioresource Technol. **312**(2020), 123615.

[5] Bridgwater A.V.: *Review of fast pyrolysis of biomass and product upgrading*. Biomass Bioenerg. **38**(2012), 68–94.

[6] Al Arni S.: *Comparison of slow and fast pyrolysis for converting biomass into fuel*. Renew. Energ. **123**(2018), 197–201.

[7] Ronsse F., Hecke S. van, Dickinson D., Prins W.: *Production and characterization of slow pyrolysis biochar: influence of feedstock type and pyrolysis conditions*. GCB Bioenergy, **5**(2013), 2, 104–115.

[8] Żabski J, Lampart P, Gumkowski S.: *Biomass drying: Experimental and numer-ical investigations*. Arch. Thermodyn. **39**(2018), 1, 39–73.

[9] Eri Q., Peng J., Zhao X.: *CFD simulation of biomass steam gasification in a fluidized bed based on a multi-composition multi-step kinetic model*. Appl. Therm. Eng. **129**(2018), 1358–1368.

[10] Xue Q., Dalluge D., Heindel T.J., Fox R.O., Brown R.C.: *Experimental val-idation and CFD modeling study of biomass fast pyrolysis in fluidized-bed reactors*. Fuel **97**(2012), 757–769.

[11] Lu L., Gao X., Shahnam M., Rogers W.A.: *Bridging particle and reactor scales in the simulation of biomass fast pyrolysis by coupling particle resolved simulation and coarse grained CFD-DEM*. Chem. Eng. Sci. **216**(2020), 115471.

[12] Liu B., Papadikis K., Gu S., Fidalgo B., Longhurst P., Li Z., Kolios A.: *CFD modelling of particle shrinkage in a fluidized bed for biomass fast pyrolysis with quadrature method of moment*. Fuel Process. Technol. **164**(2017), 51–68.

[13] Krzywański J., Sztekler K., Szubel M., Siwek T., Nowak W., Mika Ł.: *A comprehensive three-dimensional analysis of a large-scale multi-fuel cfb boiler burning coal and syngas. Part 1. The CFD model of a large-scale multi-fuel CFB combustion*. Entropy **22**(2020), 9, 1–32, 964.

[14] Krzywański J., Sztekler K., Szubel M., Siwek T., Nowak W., Mika Ł: *A comprehensive, three-dimensional analysis of a large-scale, multi-fuel, CFB boiler burning coal and syngas. Part 2. Numerical simulations of coal and syngas co-combustion*. Entropy, **22**(2020), 8, 1–30, 856.

[15] Badur J., Stajnke M., Ziółkowski P., Jóźwik P., Bojar Z., Ziółkowski P.J.: *Mathematical modeling of hydrogen production performance in thermocatalytic reactor based on the intermetallic phase of Ni3Al*. Arch. Thermodyn. **3**(2019), 3, 3–26.

[16] Kaczor Z., Buliński Z., Werle S.: *Modelling approaches to waste biomass pyrolysis: a review*. Renew. Energ. **159**(2020), 427–443.

[17] Xue Q., Heindel T.J., Fox R.O.: *A CFD model for biomass fast pyrolysis in fluidized-bed reactors*. Chem. Eng. Sci. **66**(2011), 11, 2440–2452.

[18] Yu X., Makkawi Y., Ocone R., Huard M., Briens C., Berruti F.: *A CFD study of biomass pyrolysis in a downer reactor equipped with a novel gas–solid sep-arator – I: Hydrodynamic performance*. Fuel Process. Technol. **126**(2014), 366–382.

[19] Mellin P., Zhang Q., Kantarelis E., Yang W.: *An Euler–Euler approach to modeling biomass fast pyrolysis in fluidized-bed reactors – Focusing on the gas phase*. Appl. Therm. Eng. **58**(2013), 1-2, 344–353.

[20] Qi F., Wright M.M.: *A DEM modeling of biomass fast pyrolysis in a double auger reactor*. Int. J. Heat Mass Tran. **150**(2020), 119308.

[21] Kardaś D., Hercel P., Polesek-Karczewska S., Wardach-Świecicka I.: *A novel insight into biomass pyrolysis – The process analysis by identifying timescales of heat diffusion, heating rate and reaction rate*. Energy **189**(2019), 116159.

[22] Wijaya W.Y., Kawasaki S., Watanabe H., Okazaki K.: *Damköhler number as a descriptive parameter in methanol steam reforming and its integration with absorption heat pump system*. Appl. Energ. **94**(2012), 141–147.

[23] Bidabadi M., Haghiri A., Rahbari A.: *The effect of Lewis and Damköhler num-bers on the flame propagation through micro-organic dust particles*. Int. J. Therm. Sci. **49**(2010), 3, 534–542.

[24] Ansarifar H., Shams M.: *Numerical simulation of hydrogen production by gasification of large biomass particles in high temperature fluidized bed reactor*. Int. J. Hydrogen Energ. **43**(2018), 10, 5314–5330.

[25] Nugraha M.G., Saptoadi H., Hidayat M., Andersson B., Andersson R.: *Particle modelling in biomass combustion using orthogonal collocation*. Appl. Energ. **255**(2019), 113868.

[26] Wickramaarachchi W.A.M.K.P., Narayana M.: *Pyrolysis of single biomass particle using three-dimensional Computational Fluid Dynamics modelling*. Renew. Energ. **146**(2020), 1153–1165.

[27] Wardach-Świecicka I., Kardaś D.: *Modeling of heat and mass transfer during thermal decomposition of a single solid fuel particle*. Arch. Thermodyn. **2**(2013), 2, 53–71.

[28] Gable P., Brown R.C.: *Effect of biomass heating time on bio-oil yields in a free fall fast pyrolysis reactor*. Fuel **166**(2016), 361–366.

[29] McGee H.A.: *Molecular Engineering*. McGraw Hill, New York 1991.

[30] Kuo K.K.: *Principles of Combustion*. Wiley, New York 1986.

[31] Wen C.Y., Yu Y.H.: *Mechanics of fluidization*. Chem. Eng. Prog. Sym. Ser. **62**(1966), 100–111.

[32] Ranz W.E.: *Evaporation from drops: Part II*. Chem. Eng. Progr. **48**(1952), 173–180.

[33] Ranzi E., Cuoci A., Faravelli T., Frassoldati A., Migliavacca G., Pierucci S., Sommariva S.: *Chemical kinetics of biomass pyrolysis*. Energ. Fuel. **22**(2008), 6, 4292–4300.

[34] Miller R.S, Bellan J.: *A generalized biomass pyrolysis model based on superimposed cellulose, hemicellulose and lignin kinetics*. Combust. Sci. Technol. **126**(1997), 1-6, 97–137.

[35] White J.E., Catallo W.J., Legendre B.L.: *Biomass pyrolysis kinetics: A com-parative critical review with relevant agricultural residue case studies*. J. Anal. Appl. Pyrol. **91**(2011), 1, 1–33.

[36] Rahimi Borujerdi P., Shotorban B., Mahalingam S., Weise D.R.: *Modeling of water evaporation from a shrinking moist biomass slab subject to heating: Arrhenius approach versus equilibrium approach*. Int. J. Heat Mass Tran. **145**(2019), 118672.

[37] Jin W., Singh K., Zondlo J.: *Pyrolysis kinetics of physical components of wood and wood-polymers using isoconversion method*. Agriculture **3**(2013), 1, 12–32.

[38] Ansys Fluent 12.0 Theory Guide. https://www.afs.enea.it/project/neptunius/docs/fluent/html/th/main_pre.htm (accessed 1 March 2021).

[39] Bridgwater A.V., Meier D., Radlein D.: *An overview of fast pyrolysis of biomass*. Org. Geochem. **30**(1999), 12, 1479–1493.

[40] Meier D., Faix O.: *State of the art of applied fast pyrolysis of lignocellulosic materials — a review*. Bioresource Technol. **68**(1999), 1, 71–77.

[41] Mašek O.: *Biochar in thermal and thermochemical biorefineries — production of biochar as a coproduct*. In: Handbook of Biofuels Production (2nd Edn.), (R. Luque, C. Sze Ki Lin, K. Wilson, J. Clark, Eds.), Woodhead, 2016, 655–671.

[42] Efika C.E., Onwudili J.A., Williams P.T.: *Influence of heating rates on the products of high-temperature pyrolysis of waste wood pellets and biomass model com-pounds*. Waste Manage. **76**(2018), 497–506.

[43] Klinger J.L., Westover T.L., Emerson R.M., Williams C.L., Hernandez S., Monson G.D., Ryan J.C.: *Effect of biomass type, heating rate, and sample size on microwave-enhanced fast pyrolysis product yields and qualities*. Appl. Energ. **228**(2018), 535–545.